OPEN ACCESS
JOURNAL OF ADVANCED DIELECTRICS
Vol. 13, No. 4 (2023) 2341002 (8 pages)

DOI: 10.1142/S2010135X23410023

High-accuracy characterization of pyroelectric materials: A noncontact method based on surface potential measurements

Reinhard Schwödiauer*, Simona Bauer-Gogonea and Martin Kaltenbrunner
Soft Matter Physics, Johannes Kepler University, Altenbergerstraße 69, 4040 Linz, Austria
*reinhard.schwoediauer@jku.at

Volodymyr Tkachenko and Simonetta Grilli
Institute of Applied Sciences & Intelligent Systems, National Research Council (CNR-ISASI)
Via Campi Flegrei 34, 80078 Pozzuoli (NA), Italy

Received 26 September 2022; Revised 25 November 2022; Accepted 7 February 2023; Published 6 May 2023

The characterization of pyroelectric materials is essential for the design of pyroelectric-based devices. Pyroelectric current measurement is the commonly employed method, but can be complex and requires surface electrodes. Here, we present noncontact electrostatic voltmeter measurements as a simple but highly accurate alternative, by assessing thermally-induced pyroelectric surface potential variations. We introduce a refined model that relates the surface potential variations to both the pyroelectric coefficient and the characteristic figure of merit (FOM) and test the model with square-shaped samples made from PVDF, $LiNbO_3$ and $LiTaO_3$. The characteristic pyroelectric coefficient for PVDF, $LiNbO_3$ and $LiTaO_3$ was found to be 33.4, 59.9 and 208.4 $\mu C\ m^{-2}\ K^{-1}$, respectively. These values are in perfect agreement with literature values, and they differ by less than 2.5% from values that we have obtained with standard pyroelectric current measurements for comparison.

Keywords: Pyroelectric coefficient; surface potential; figure of merit.

1. Introduction

Pyroelectricity is the temporal temperature gradient response of the spontaneous polarization in pyroelectric materials.[1] Such pyroelectric materials constitute a special class of functional materials, which are widely used in infrared detection and imaging,[2–5] for thermal waste heat harvesting,[6,7] X-ray generation,[8,9] electron emission,[10] neutron generation[11,12] and possible nuclear fusion experiments,[13] as well as for pyroelectro-hydrodynamic micro droplet dispensing.[14,15] The diversity of possible application is supported by the diversity of pyroelectric crystals, ceramics or polymer foils and thin films.[16,17] Altogether, they span a remarkable large range of different mechanical, electrical and thermal properties.

The characteristic property of all pyroelectrics is the pyroelectric coefficient, $p = dP_s/dT$, describing the change of the spontaneous polarization P_s, due to a change in temperature T. The pyroelectric coefficient can be assessed in various ways. A literature review[18] published in 2017, identified 19 different techniques based on electrical, optical, thermal or radiative measured quantities. Irrespective of the variety of techniques, the accurate determination of p requires great care regarding the experimental method and the analysis of the measured data. By comparison, a fairly limited experimental effort is associated with electrical techniques which primarily use an electrometer to measure voltage, charge, or current. Such measurements, however, need electrodes which in some cases require considerable effort to manufacture. Especially in the case of already polarized, temperature-sensitive pyroelectrics with low Curie temperature (PVDF, $BaTiO_3$, etc.), conventional electrode coating by physical vapor deposition is problematic, as the polarization decreases due to the thermal stress.

An interesting but rarely used alternative to electrometer measurements is a contactless voltage measurement with an electrostatic voltmeter. A contactless measurement allows for a surface mapping of a pyroelectric, wherever pyroelectric materials shall be used without surface electrodes in order to generate a high external electric field strength. Schein *et al*.[19] first published measurements with an electrostatic voltmeter on $LiNbO_3$ crystals to observe optical damage via the associated effect of electrostatic charge separation. Two subsequent papers[20,21] further demonstrated the use of an electrostatic voltmeter to determine the secondary and tertiary pyroelectric coefficient of partially clamped $LiNbO_3$ crystals. The secondary coefficient is associated with the deformation of the material, while the tertiary coefficient is related to the temperature gradient within the specimen. The primary pyroelectric coefficient has to be determined under the condition of constant strain, which is most difficult to achieve experimentally. In

*Corresponding author.

contrast, measurements under the condition of constant stress are easy to perform. For unstrained samples, the measurements therefore predominantly yield an effective pyroelectric coefficient (the sum of primary, secondary and tertiary effects). From a practical point of view, it is often sufficient to characterize and to compare the effective pyroelectric coefficient of different unknown samples.

In this work, we introduce a method for a noncontact high-accuracy assessment of the effective pyroelectric coefficient with an electrostatic voltmeter. For this purpose, we extend the investigation of Schein *et al*. with an improved model calculation considering the specific finite circular and square geometry of the pyroelectric sample. We present high-accuracy electrostatic voltmeter measurements and relate the surface potential variations to important metrics like the voltage figure of merit (FOM) and the effective pyroelectric coefficient. The contactless technique necessitates no surface electrodes and careful guarding measures to prevent leakage currents can be omitted. Therefore, the presented technique shows particular advantages over its alternatives. The improved model developed for a circular or a quadratic thin pyroelectric plate directly yields the voltage FOM, $F_v = p/\varepsilon$. The only required parameters are the two easily accessible geometric quantities for thickness and surface area. The experimental input data consists of temperature difference and the corresponding surface potential difference. We used three different pyroelectric materials — PVDF, $LiNbO_3$ and $LiTaO_3$ — all showing different values for surface area and thickness, to conduct the transient surface potential measurements caused by sinusoidal temperature variations. These contactless potential measurements are compared with typical standard electrometer measurements of the very same samples with surface electrodes. Additional measurements of the dielectric permittivity, ε, allow the comparison between the voltage FOM and the effective pyroelectric coefficient for both measurement techniques. The high degree of agreement proves the model as an excellent approximation, especially for thin samples with a sufficiently small thickness-to-area ratio. We further estimate the error of our approximation by numerical finite element method (FEM) calculations.

2. Surface Potential of Thin Pyroelectrics

In general, the fringing field at the edges of a finite pyroelectric plate noticeably affects the overall electric field, and thus also the associated surface potential. This prevents an exact description of the surface potential with a closed algebraic formula. However, a very precise and simple approximation can be derived for many practical cases if following conditions apply:

(i) The pyroelectric sample has a flat surface with a circular or quadratic geometry, and the thickness is sufficiently small compared to the lateral dimension.
(ii) The orientation of the spontaneous polarization is normal to the flat surface of the pyroelectric sample.
(iii) The polarization of the pyroelectric sample is homogeneous throughout the pyroelectric sample volume.

With these conditions, the spontaneous polarization can be replaced by a constant surface charge density of opposite polarity for the two sides:

$$\sigma = \pm P_s. \tag{1}$$

2.1. *Circular pyroelectric plate*

A disk- shaped pyroelectric with radius R, and polarization P_S oriented in positive z-direction carries a positive charge density σ on the circular top surface, as shown in Fig. 1(a). The electric potential, ϕ_C, along the central z-axis of such a circular charge distribution is as follows:[22,23]

$$\phi_C(z) = \frac{\sigma}{2\varepsilon_0}\left(\sqrt{R^2+z^2} - R - |z|\right), \tag{2}$$

where ε_0 denotes the permittivity of vacuum. The superposition of two opposite surface charges separated by the thickness s results in the electric potential of a polarized

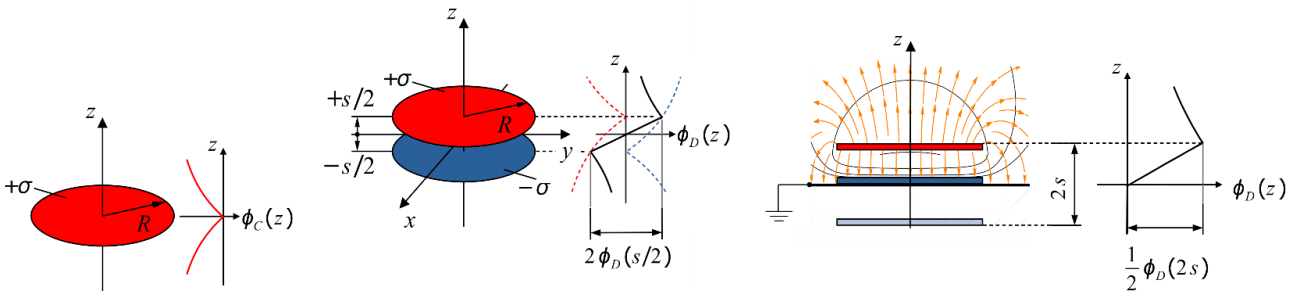

Fig. 1. The central surface potential of a polarized disk with $\varepsilon = 1$ on a grounded metal platform. (a) The potential of a circular positive charge density is (b) superimposed with the potential of a similar negative charge density. (c) The placement on a grounded metal base produces an image charge, which effectively doubles the thickness of the polarized disk.

disk (Fig. 1(b)) with the permittivity of $\varepsilon = 1$. The electric potential of the polarized disk along the z-axis results in $\phi_D(z) = \phi_C(z - s/2) - \phi_C(z + s/2)$, and the total surface potential difference yields $\Delta\phi_D(s) = 2\phi_D(s/2)$.

If the disk in Fig. 1(b) is placed on a grounded flat metal base (Fig. 1(c)), the surface potential changes. The field lines are forced to normal orientation at the metal surface which acts like a mirror, both for field lines and charges. This effectively doubles the separation between the upper surface charge and its image from s to $2s$. The opposite surface charge rests on the metal surface and is essentially canceled by its adjacent image. Therefore, the central surface potential is described with $\phi_D(2s)/2$.

These considerations are valid for $\varepsilon = 1$. For real pyroelectric disks with $\varepsilon > 1$, the central surface potential difference can only be determined numerically by FEM. However, an analytical approximation can be expressed by

$$\Delta\phi_S \approx \frac{\phi_D(2s)}{2\varepsilon} = \frac{\sigma}{2\varepsilon\varepsilon_0}\left(R + 2s - \sqrt{R^2 + 4s^2}\right). \tag{3}$$

This approximation ignores the continuity conditions for the electric- and dielectric-displacement fields at the edges. The values obtained therefore increasingly deviate from the accurate surface potential as the s/R-ratio increases. In many practical cases, however, s/R is sufficiently small so that the error becomes largely negligible. For these cases, Eq. (3) accurately describes the surface potential measured by an electrostatic voltmeter with its sensor positioned at the center above the top surface of a thin pyroelectric disk on a grounded platform. In the limit of an infinite radius, Eq. (3) reduces to the generally well-known term $\Delta\phi_S = \sigma s/\varepsilon\varepsilon_0$, used by Schein *et al.*[19] for the calculation of the pyroelectric coefficient.

The surface potential in Eq. (3) directly relates to the pyroelectric coefficient via Eq. (1). A simple algebraic rearrangement yields the following:

$$p = \frac{2\varepsilon\varepsilon_0}{R + 2s - \sqrt{R^2 + 4s^2}} \frac{\Delta\phi_S}{\Delta T}. \tag{4}$$

This expression links the voltage FOM, $F_V = p/\varepsilon$, to a simple contactless measurement of the temperature-dependent surface potential. The purely geometric proportionality factor is directly accessible. Additional material parameters are not required.

2.2. *Quadratic pyroelectric plate*

In complete analogy to the discussion above, we extend the model in Eq. (3) to a thin quadratic pyroelectric plate. However, the final algebraic expression is considerably more complicated. As outlined in the appendix, a quadratic charge distribution with finite side length a produces a potential along the symmetry line which is described by

$$\phi_Q(z) = -\frac{\sigma}{\pi\varepsilon_0}\left[z\,\mathrm{arccot}\frac{2z\sqrt{\frac{a^2}{2} + z^2}}{\frac{a^2}{2}} + \ldots \right.$$
$$\left. \ldots + a\left(\mathrm{arctanh}\sqrt{2} - \mathrm{arctanh}\frac{\sqrt{\frac{a^2}{2} + z^2}}{\frac{a}{2}} \right) \right]. \tag{5}$$

Compared to Eq. (2), Eq. (5) is more complex and difficult to handle. However, the numerical difference is almost insignificant, if the areas a^2 and πR^2 are sufficiently similar in size, i.e., if $a/R \sim \sqrt{\pi} = 1.7725$. In particular, the error $1 - \phi_C(z)/\phi_Q(z)$ can be empirically reduced to a minimal value of <0.007% for a value of $a/R = 1.799$, which is about 1.5% larger than $\sqrt{\pi}$. This theoretical result proves important for the experimental design, since quadratic samples can be easily prepared by cutting. In practical applications, measurements are therefore performed on samples with a quadratic geometry more often than on circular-shaped samples.

2.3. *FEM error calculation*

The approximated surface potential $\Delta\phi_S$ in Eq. (3) deviates from the accurate surface potential value of a quadratic plate, $\Delta\varphi_S$, which can be calculated only numerically by FEM. With these results, the error of $\Delta\phi_S$ is expressed by

$$\mathrm{err}_\phi = 1 - \frac{\Delta\phi_S}{\Delta\varphi_S}. \tag{6}$$

The plot of err_ϕ versus permittivity is depicted in Fig. 2 for different values of the dimensionless parameter s/a.

The data reveal a functional relationship, which can be reasonably well described by the empirical fit function:

$$\mathrm{err}_\phi \cong 0.89\left(1 - \frac{1}{\varepsilon}\right)^{0.9} \frac{s}{a}, \tag{7}$$

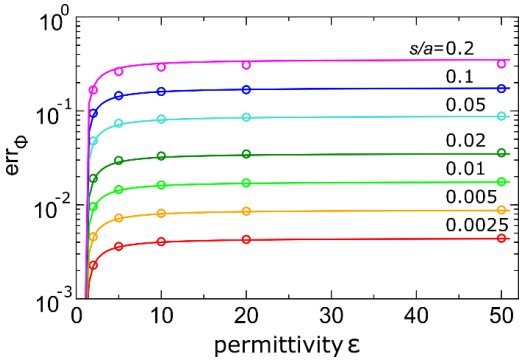

Fig. 2. Modeling of a quadratic pyroelectric plate. Data points display the error between the approximated surface potential $\Delta\phi_S$, according to Eq. (3), and the FEM calculated surface potential value $\Delta\varphi_S$. The solid lines represent an empiric fit according to Eq. (7).

shown in Fig. 2 as solid lines. The agreement of this fit function with the calculated error data is best for small *s/a*-ratios and starts to deviate noticeable for $s/a \geq 0.2$. An error below 10% can be expected for *s/a*- ratios below 1/9. The actual experimental error, however, may deviate from the estimation significantly since the edges of a real pyroelectric sample are often far from a perfect vertical boundary. Small cracks, tiny broken-out splinters and other edge-defects can affect the surface potential and produce additional errors for which Eq. (7) does not account for. Due to these issues, Eq. (7) not necessarily improves the accuracy of Eq. (3) any further.

3. Experimental

Experimental measurements with an electrostatic voltmeter, and comparative measurements with an electrometer were performed on quadratic pyroelectric samples with different *s/a* ratios. For the experiments we prepared samples made from PVDF (s =120 μm, a =10 and 20 mm, respectively), $LiNbO_3$ (s = 0.5 mm, a = 20 mm), and $LiTaO_3$ (s = 0.52 mm, a = 10 mm). We coated one side of every sample surface with conductive silver paste in order to define an equipotential reference surface. This conductive layer also was in electrical contact to a thin copper wire placed close to a sample edge. As illustrated in Fig. 3(a), we softly attached the previously coated sample surface with a thermal conduction paste to a 1 mm thick aluminum support, which was further adhered to a Peltier Module. The aluminum support exposes and raises the copper wire contact from the supporting surface of the Peltier Module and thus allows for a planar alignment. We covered the upper surface of the Peltier Module with a thin copper tape that both serves as an extended equipotential reference surface, and additionally shields the measurement zone from possible signal noise induced by the module below. Altogether, the Peltier Module with the sample is located in a closed electrically grounded metal housing with electrical feedthroughs, as depicted in Fig. 3(b). For the contactless voltage measurements with a Monroe 244A Isoprobe Electrostatic Voltmeter, we connected the equipotential surfaces to common ground and positioned the sensing Kelvin probe *ca*. 0.5 mm above the electrode-free sample surface.

For the comparative electrometer measurements with a Keithley 6514 System Electrometer, we modified the setup slightly according to Fig. 3(c). We further equipped the sample surface with a silver paste electrode by means of a quadratic shadow mask. This top electrode, connected to HI-input of the electrometer, was *ca*. 20% smaller than the full sample surface area. The bottom silver paste layer was connected to the LO-input with a zero-potential reference to common ground.

In both experimental arrangements, the Peltier Module was driven with a custom-made power supply, providing a constant harmonically oscillating driving voltage with a frequency of 5 mHz. This produces a sinusoidal temperature variation of about ±1.5°C with respect to room temperature. A fan and a heat sink ensured that the thermal equilibrium is maintained at room temperature. We sensed the actual temperature of the sample with a type-K fine gauge thermocouple with 0.003'' conductors, attached via a tiny drop of silver paste near a corner of the upper sample surface. The temperature was passively measured with a Eurotherm 902 controller.

4. Results and Discussion

A complete set of measured and calculated data for the $LiNbO_3$ sample is presented with the diagrams in Fig. 4. For reference purpose, we first studied the pyroelectric current with electrometer measurements. Figure 4(a) shows the time course of the pyroelectric current over three cycles with a peak value of *ca*. $I_P \approx 610$ pA. This current, related to an electrode area of $A = (15.5 \text{ mm})^2$, is caused by the sinusoidal temperature variation centered at 24° C with a frequency $f = 5$ mHz and an amplitude $T_a \approx 1.3$°C.

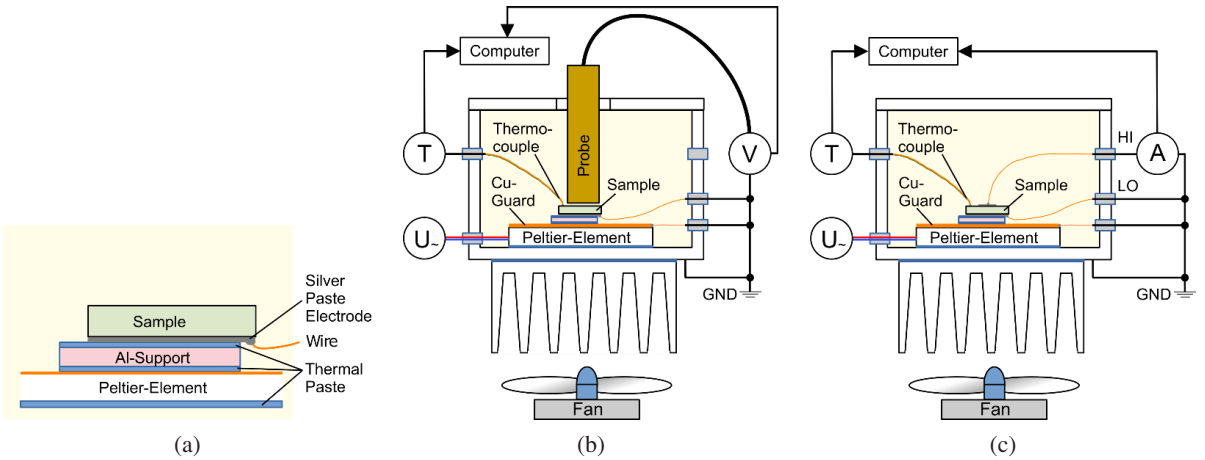

(a) (b) (c)

Fig. 3. (a) Illustration of the pyroelectric sample arrangement, (b) experimental setup for contactless measurements with an electrostatic voltmeter and (c) for comparative current measurements with an electrometer.

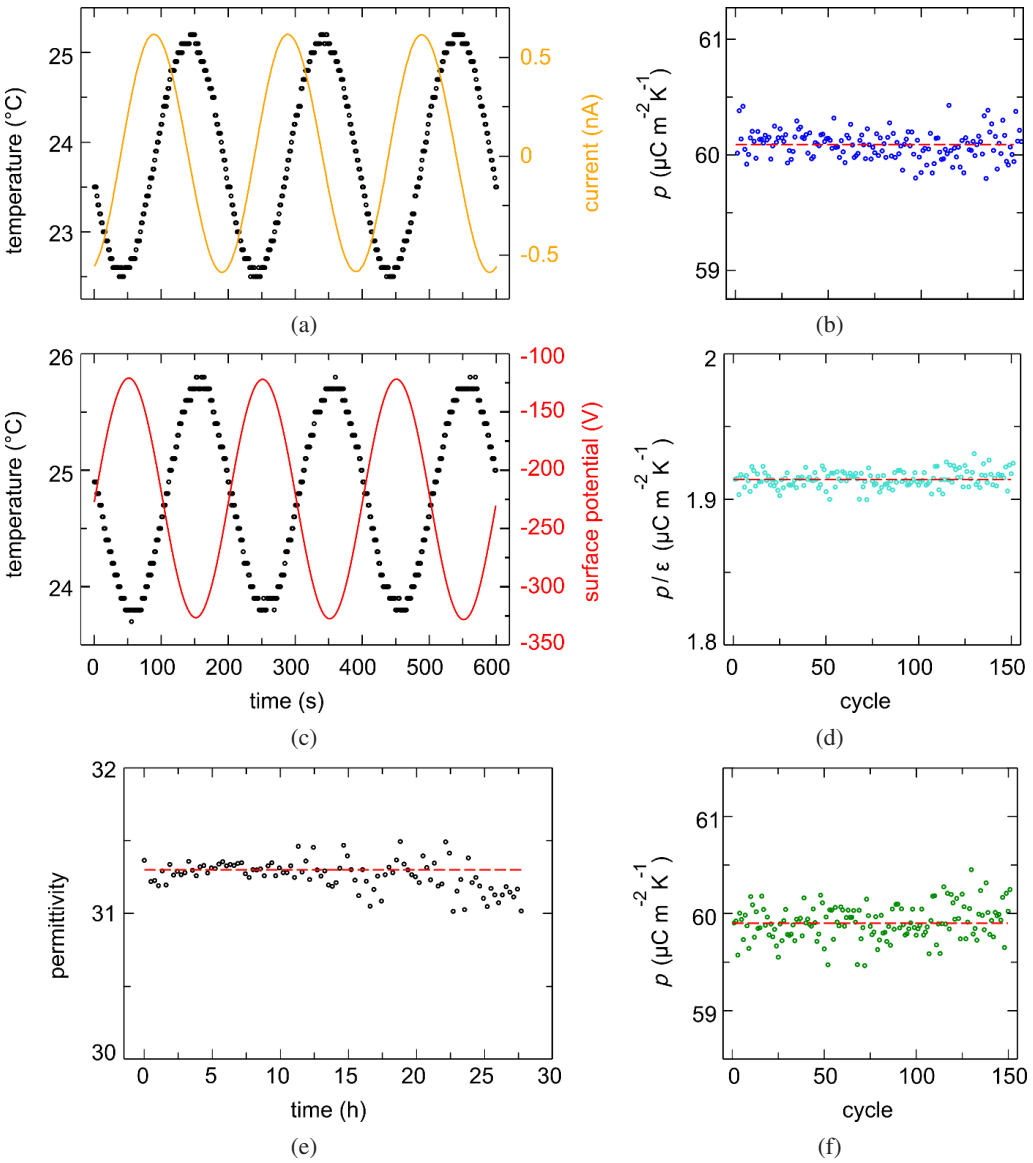

Fig. 4. Measured and calculated data set for the $LiNbO_3$ sample. (a) The pyroelectric current (solid line) due to the harmonic temperature variation (scattered data points), yields (b) a pyroelectric coefficient of 60.1 ± 0.12 μC m^{-2} K^{-1}. (c) The surface potential (solid line), caused by the harmonic temperature variation (scattered data points), yields (d) a voltage figure of merit of 1.91 ± 0.01 μC m^{-2} K^{-1}. (e) With the measured permittivity of 31.3 ± 0.1, a mean pyroelectric coefficient (f) of 59.9 μC m^{-2} K^{-1} is obtained. The deviation between the mean values in (b) and (f) amounts to only 0.3%.

With these values, we obtain the pyroelectric coefficient for every cycle[18]

$$p = \frac{I_p}{2\pi f A T_a}. \tag{8}$$

The calculated values of 154 cycles are displayed in Fig. 4(b) as scattered data points around a mean value of p = 60.09 μC m^{-2} K^{-1} (dashed line) with a standard deviation of 0.12 μC m^{-2} K^{-1}. This value agrees almost perfectly with declared precision measurements of an undoped $LiNbO_3$ crystal,[24] and it is well in the range between 40 and 96 μC m^{-2}K^{-1} as reported in the literature.[5,7,25]

In order to test our model, we perform surface potential tests shown in Fig. 4(c). Again, the sample is subjected to a 5 mHz sinusoidal temperature variation of $T_a \approx 2$°C, centered around 24.8°C. The related surface potential difference of $\Delta\phi_S \approx 207$ V is centered at about −225 V. This shift can be attributed to a slightly positive temperature difference before and after mounting the $LiNbO_3$ sample.

With the ratio $\Delta\phi_S/\Delta T$ from Fig. 4(c), and the geometric parameters sample thickness, s = 0.5 mm, and side length, a = 20 mm, we calculate the voltage FOM from Eq. (4) and display the data as scattered data points in Fig. 4(d). The mean voltage FOM from 151 consecutive temperature cycles

is $F_V = \langle p/\varepsilon \rangle = 1.91$ μC m^{-2}K^{-1} (dashed line) with a standard deviation of ±0.01 μC m^{-2}K^{-1}. In order to determine the pyroelectric coefficient from the FOM data, the permittivity of the sample has to be known. Respective data in the literature are available mostly for higher frequencies like 100 Hz or 1 kHz, therefore we measured the permittivity values of our samples for the experimental frequency of 5 mHz with a Novocontrol Alpha-A Impedance Analyzer. Impedance measurements of pyroelectrics at such low frequencies require both a sufficient temperature stability and little electromagnetic interference. Thus, measurements during the night time can significantly reduce statistical scatter of measured permittivity values. This is evident in Fig. 4(e) where the data of the first 10 h measurement during the night time shows a significantly smaller deviation from the mean permittivity value of $\langle \varepsilon \rangle = 31.3$ (dashed line). Both $\langle \varepsilon \rangle$ and the standard deviation of about 0.1 include all 100 data points that were recorded during the full 28 h of testing. With the measurement of the low-frequency dielectric constant, it is now possible to represent the voltage FOM data as measured values for the pyroelectric coefficient. The respective scattered data points are graphed in the diagram of Fig. 4(f) showing a mean value of $\langle p \rangle = 59.9$ μC m^{-2}K^{-1} (dashed line) with a standard deviation of 0.18 μC m^{-2}K^{-1}. This result deviates from the standard pyroelectric current measurements by just 0.3%. This small error is well within the experimental accuracy. The error margin between the different methods of measurement is equally small also for the other three samples.

The bar chart in Fig. 5 shows the pyroelectric coefficients for all four samples and compares the respective results from the standard current measurement, represented by the left, dotted bars, and from the surface potential measurement, represented by the right, hatched bars.

Table 1 includes a more detailed presentation of the measurement results for all samples. The pyroelectric coefficients

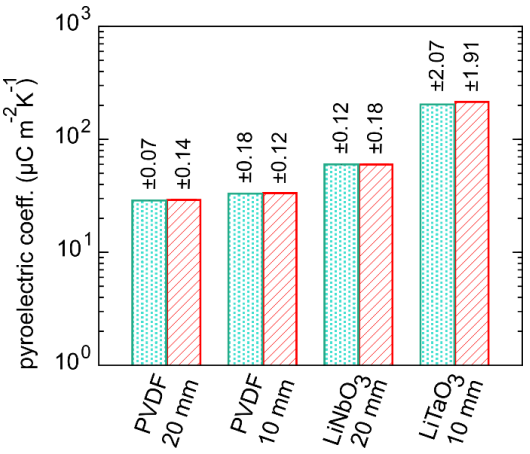

Fig. 5. Pyroelectric coefficient for different materials obtained with standard current measurements (left, dotted bar) and with surface potential measurements (right, hatched bar). The numbers above the bars represent the standard deviations of the respective data.

Table 1. List of parameters, measured data, calculated mean values and standard deviations for the four pyroelectric samples under investigation. The list includes the parameters for side length, a and sample thickness, s, permittivity, ε, the mean temperature and temperature amplitude, $T_I \pm T_a$, for the current measurement, the peak current, I_P, the mean temperature and temperature amplitude, $T_\phi \pm T_a$, for the surface potential measurement, the surface potential difference $\Delta\phi_S$, the voltage FOM F_V, the pyroelectric coefficient, p_I, obtained from standard current measurements, the pyroelectric coefficient, p_ϕ, obtained from surface potential measurements, and the error between the two coefficients.

	Polymer		Crystals	
Parameters	PVDF	PVDF	$LiNbO_3$	$LiTaO_3$
a (mm)	20	10	20	10
s (μm)	120	120	500	521
$T_I \pm T_a$ (°C)	23.17±1.4	23.67±1.4	24.07±1.33	24.77±3.2
I_P (pA)	126.63±2.87	71.20±2.85	610.36±24.78	1028.3±5.91
$T\phi \pm T_a$ (°C)	23.26±1.2	24.22±1.3	24.78±1.0	24.41±1.5
$\Delta\phi_S$ (V)	70.0±0.4	76.2±0.3	206.6±1.1	320.4±2.2
F_V (μC m^{-2}K^{-1})	2.18±0.01	2.21±0.01	1.91±0.01	4.04
ε	13.34±0.1	15.13±0.1	31.26±0.1	53.10±1.7
$p\phi$ (μC m^{-2}K^{-1})	29.02±0.14	33.40±0.12	59.91±0.18	208.4±3.69
p_I (μC m^{-2}K^{-1})	28.81±0.07	33.11±0.18	60.09±0.12	203.6±2.07
$1 - p\phi/p_I$	**−0.007**	**−0.009**	**0.003**	**−0.024**

obtained from standard current measurements, p_I, are denoted in the second-last line as mean values and standard deviations. Similar to $LiNbO_3$, there is a good agreement with literature values for PVDF (24–33 μC m^{-2}K^{-1})[6,26,27] and $LiTaO_3$ (176–230 μC m^{-2}K^{-1}).[4,5,28] Also included are the pyroelectric coefficients obtained from the surface potential measurements p_ϕ. The last line in Table 1 shows the error between both measurement results. The largest error of about 2.5% is found for the $LiTaO_3$ sample, which has the largest s/a ratio. This error is nevertheless reasonably small for most practical applications.

5. Conclusion

We have demonstrated that characteristic voltage FOM values for pyroelectrics can be obtained directly and with high accuracy from contactless surface potential measurements using an electrostatic voltmeter. Such measurements require little experimental effort; they act like an ideal measurement with an infinitely high input resistance and with a complete absence of any leakage currents. Careful guarding and shielding measures are not required. The voltage signal is easily accessible in a region between 10 and several 100 volts. We introduced and tested a model that relates the surface potential data to both the pyroelectric coefficient and the characteristic FOM. If the sample permittivity is known, the pyroelectric coefficient can be determined from the voltage

FOM, with an accuracy that is comparable to standard current measurements.

In reverse, if the pyroelectric coefficient is known, the introduced method can be used to evaluate the low-frequency permittivity, which is tedious to measure. The suggested approach works for flat, circular and quadratic samples with a homogeneous polarization normal to the surface, and a thickness-to-diameter ratio <1/10.

Acknowledgments

This work was supported by the European Horizon 2020 grant "SensApp" under Grant Agreement No. 829104.

Appendix A. Central Field and Potential of a Quadratic Pyroelectric Plate

The central electric field of a quadratic plate of side length a, with a positive charge density σ, is schematically depicted in Fig. A.1. A differential charge element, $dQ = \sigma dx dy$ at position $\vec{r}_\sigma$ causes at position $\vec{r} = z\hat{e}_z$ a differential field strength

$$dE_z = \frac{\sigma}{4\pi\varepsilon_0}\frac{z\, dx\, dy}{\left(x^2+y^2+z^2\right)^{3/2}}. \tag{A.1}$$

Integration yields:

$$E_z(z) = \frac{\sigma}{\pi\varepsilon_0}\operatorname{arccot}\left(\frac{2z\sqrt{a^2/2+z^2}}{a^2/2}\right). \tag{A.2}$$

Since the electric field and the potential along the z-axis are related by $E_z = -d\phi_Q(z)/dz$, one obtains the following expression:

$$\begin{aligned}\phi_Q(z) &= -\int_0^z E_z(\zeta)\,d\zeta \\ &= -\frac{\sigma}{\pi\varepsilon_0}\left[z\operatorname{arccot}\frac{2z\sqrt{\frac{a^2}{2}+z^2}}{\frac{a^2}{2}}+\ldots\right. \\ &\left.\ldots+a\left(\operatorname{arctanh}\sqrt{2}-\operatorname{arctanh}\frac{\sqrt{\frac{a^2}{2}+z^2}}{\frac{a}{2}}\right)\right].\end{aligned} \tag{A.3}$$

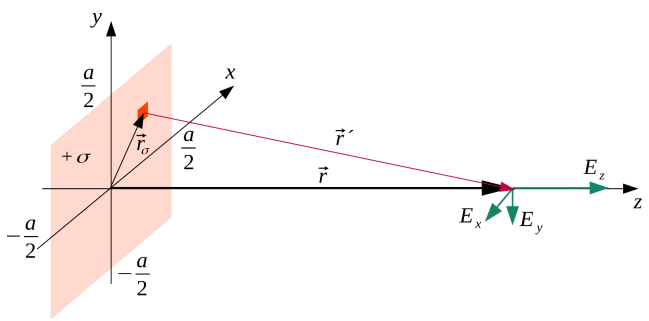

Fig. A.1. Electric field calculation of a quadratic plate with positive surface charge density.

References

[1] S. B. Lang, Pyroelectricity: From ancient curiosity to modern imaging tool, *Phys. Today* **58**, 31 (2005).
[2] A. J. Holden, Pyroelectric sensor arrays for detection and thermal imaging, *Proc. SPIE: Infrared Technol. Appl. XXXIX*, **8704**, 483 (2013).
[3] A. Rogalski, Infrared detectors: An overview, *Infrared Phys. Technol.* **43**, 187 (2002).
[4] M. H. Lee, R. Guo and A. S. Bhalla, Pyroelectric sensors, *J. Electroceram.* **2**, 229 (1998).
[5] H. P. Beerman, Investigation of pyroelectric material characteristics for improved infrared detector performance, *Infrared Phys.* **15**, 225 (1975).
[6] S. P. Alpay, J. Mantese, S. Trolier-McKinstry, Q. Zhang and R. W. Whatmore, Next-generation electrocaloric and pyroelectric materials for solid-state electrothermal energy interconversion, *MRS Bull.* **39**, 1099 (2014).
[7] C. R. Bowen, J. Taylor, E. LeBoulbar, D. Zabek, A. Chauhan and R. Vaish, Pyroelectric materials and devices for energy harvesting applications, *Energy Environ. Sci.* **7**, 3836 (2014).
[8] J. D. Brownridge, Pyroelectric x-ray generator, *Nature* **358**, 287 (1992).
[9] S. Imashuku, Technology of pyroelectric x-ray tubes, *Handbook of X- ray Imaging, Physics and Technology*, ed. P. Russo (CRC Press, Boca Raton, 2018), pp. 131–138.
[10] G. Rosenman, D. Shur, Y. E. Krasik and A. Dunaevsky, Electron emission from ferroelectrics, *J. Appl. Phys.* **88**, 6109 (2000).
[11] B. Naranjo, J. Gimzewski and S. Putterman, Observation of nuclear fusion driven by a pyroelectric crystal, *Nature* **434**, 1115 (2005).
[12] Y. Danon, Pyroelectric crystal d-d and d-t neutron generators, *J. Instrum.* **7**, C04002 (2012).
[13] W. Tornow, Production of 14 MeV neutrons using pyroelectric crystals: Reconverting solar energy into nuclear fusion energy, *Int. J. Energy Sci.* **4**, 101 (2014).
[14] P. Ferraro, S. Coppola, S. Grilli, M. Paturzo and V. Vespini, Dispensing nano–pico droplets and liquid patterning by pyroelectrodynamic shooting, *Nat. Nanotechnol.* **5**, 429 (2010).
[15] S. Grilli, L. Miccio, O. Gennari, S. Coppola, V. Vespini, L. Battista, P. Orlando and P. Ferraro, Active accumulation of very diluted biomolecules by nano-dispensing for easy detection below the femtomolar range, *Nat. Commun.* **5314** (2014), doi:10.1038/ncomms6314.
[16] D. Zhang, H. Wu, C. R. Bowen and Y. Yang, Recent advances in pyro- electric materials and applications, *Small* **17**, 2103960 (2021).
[17] G. Velarde, S. Pandya, J. Karthik, D. Pesquera and L. W. Martin, Pyroelectric thin films—past, present, and future, *APL Mater.* **9**, 010702 (2021).
[18] S. Jachalke, E. Mehner, H. Stöcker, J. Hanzig, M. Sonntag, T. Weigel, T. Leisegang and D. C. Meyer, How to measure the pyroelectric coefficient? *Appl. Phys. Rev.* **4**, 021303 (2017).
[19] L. B. Schein, P. J. Cressman and F. M. Tesche, Electrostatic observations of laser-induced optical damage in $LiNbO_3$, *J. Appl. Phys.* **48**, 4844 (1977).
[20] L. B. Schein, P. J. Cressman and L. E. Cross, Electrostatic measurements of unusually large secondary pyroelectricity in partially clamped $LiNbO_3$, *Ferroelectrics* **22**, 937 (1978).
[21] L. B. Schein, P. J. Cressman and L. E. Cross, Electrostatic measurements of tertiary pyroelectricity in partially clamped $LiNbO_3$, *Ferroelectrics* **22**, 945 (1978).
[22] D. Halliday, R. Resnick and J. Walker, *Fundamentals of Physics Extended*, 10th edn. (John Wiley & Sons, Inc., 2014), p. 789.
[23] T. Moore, *Six Ideas That Shaped Physics: Unit E - Electromagnetic Fields* (McGraw-Hill, 2016), p. 59.

[24]T. Bartholomäus, K. Buse, C. Deuper and E. Krätzig, Pyroelectric coefficients of $LiNbO_3$ crystals of different compositions, *Phys. Status Solidi A* **142**, K55 (1994).
[25]S. T. Popescu, A. Petris and V. I. Vlad, Interferometric measurement of the pyroelectric coefficient in lithium niobate, *J. Appl. Phys.* **113**, 043101 (2013).
[26]J. G. Bergman, J. H. McFee and G. R. Crane, Pyroelectricity and optical second harmonic generation in polyvinylidene fluoride films, *Appl. Phys. Lett.* **18**, 203 (1971).
[27]G. Sebald, D. Guyomar and A. Agbossou, On thermoelectric and pyroelectric energy harvesting, *Smart Mater. Struct.* **18**, 125006 (2009).
[28]A. M. Glass, Dielectric, thermal, and pyroelectric properties ferroelectric $LiTaO_3$, *Phys. Rev.* **172**, 564 (1968).